

Contents lists available at ScienceDirect

International Journal of Solids and Structures

journal homepage: www.elsevier.com/locate/ijsolstr





Effect of pre-strain on springback behavior after bending in AA 6016-T4: Experiments and crystal plasticity modeling

Dane Sargeant ^a, Md Zahidul Sarkar ^b, Rishabh Sharma ^c, Marko Knezevic ^b, David T. Fullwood ^c, Michael P. Miles ^a, *

- ^a Department of Manufacturing Engineering, Brigham Young University, Provo, UT 84602, United States
- ^b Department of Mechanical Engineering, University of New Hampshire, Durham, NH 03824, United States
- ^c Department of Mechanical Engineering, Brigham Young University, Provo, UT 84602, United States

ARTICLE INFO

Keywords: Aluminum alloys Backstress fields Springback Springforward Strain path changes

ABSTRACT

Modeling springback in sheet materials is challenging in aluminum alloys, especially when a complex strain path is applied. This paper presents results from pure bending experiments on AA 6016-T4 sheet material, where various plastic pre-strains were first applied prior to bending. A crystal plasticity based elasto-plastic self-consistent (EPSC) model that includes the effect of backstress in the hardening law was used to predict final part shape after unloading. The backstress term in the model was calibrated using geometrically necessary dislocation (GND) content, measured experimentally by high resolution electron backscattered diffraction (HREBSD). The EPSC model predicted springforward angles for unstrained 1 mm AA 6016-T4 sheet with an error of 0.4% (0.3°) in the worst case, while the J2 plasticity isotropic model overpredicted springforward angles by as much as 2.4% (2°). For cases where uniaxial, plane-strain, and biaxial pre-strains were first imparted to the sheets before bending, the EPSC model with backstress accurately predicted the transition from springforward to springback, while the EPSC model without backstress did not. Backstress influence on model accuracy, which increased with greater pre-strain levels, appears to be correlated to the statistically stored dislocation (SSD) density computed by the model at the end of each pre-strain step.

1. INTRODUCTION

In the automotive industry, stamped parts often require multi-step forming operations to manufacture complicated geometries. During these deformation processes, complex interactions arise between dislocation hardening processes and the evolution of internal stresses that vary with strain path, and strongly influence backstresses that manifest in the form of springback during unloading (Boers et al., 2010). The absence of long-range internal stresses in typical isotropic hardening laws leads to difficulty in predicting final part geometry via standard simulation frameworks. As the strain path can often be very different as a function of location within a complex part, it is critical that combined hardening and internal stress behavior be characterized using both macro and micro approaches to fully understand its impact on springback. The current study analyzes springback in AA6016-T4 sheets during a standard bending operation, following various initial pre-strain deformations (biaxial, plane-strain, and uniaxial tension). The modeling component employs a strain path sensitive anisotropic hardening and

backstress enabled crystal plasticity elasto-plastic self-consistent (EPSC) model to overcome some of the deficiencies in previous models, in order to accurately predict the final springback. The EPSC simulations are also compared with a simple isotropic hardening law, to highlight the importance of incorporating dislocation-based hardening and backstress in order to predict elastic unloading and final part shape after forming.

The springback behavior in high strength 6xxx or 7xxx series aluminum can be understood by considering the precipitate-based microstructures in these alloys, and associated dislocation substructures (Al-Harbi et al., 2010; El-Madhoun et al., 2003; Knezevic and Beyerlein, 2018; Moan and Embury, 1979; Stoltz and Pelloux, 1974; Stoltz and Pelloux, 1976). Long-range internal stress development is associated with the presence of geometrically necessary dislocations (GNDs) that form to maintain strain compatibility during deformation (Ashby, 1970), that accumulate in pileups at obstacles such as grain boundaries (GBs) or precipitates (Shen et al., 1988), or that are associated with substructures within grains (Field et al., 2005). Backstresses build up in the strain gradient regions, due to the interaction between dislocations

E-mail address: mmiles@byu.edu (M.P. Miles).

^{*} Corresponding author.

of the same polarity and contribute to the cumulative hardening behavior of the alloy by opposing the applied resolved shear stress necessary for dislocation slip. However, they also assist dislocation slip upon reversal, or change in strain path, causing nonlinear unloading and softening and/or lower subsequent yield stresses (Bauschinger effect).

In a recent study in AA6016-T4 sheet, GND content was measured by high resolution electron backscatter diffraction (HREBSD), after prestraining the material in biaxial, plane-strain and uniaxial tension. Backstress levels estimated using these experimentally measured GND were shown to have a significant effect on the elasto-plastic transition and plastic response under subsequent uniaxial tension deformation (Sharma et al., 2022). Additional studies that included cyclic deformation cycles and various pre-strain conditions in advanced high strength steel (AHSS) alloys and a 7xxx series aluminum showed a decrement in elastic modulus values upon unloading-reloading, and an increase in springback with greater pre-strain levels (Ardeljan et al., 2016; Chongthairungruang et al., 2012; Knezevic et al., 2013a; Yoshida et al., 2002; Yue et al., 2018). The importance of including the inelastic recovery, i.e., the drop in elastic modulus after the plastic deformation of the metal alloy, as an important parameter in the prediction of springback has been highlighted previously (Chongthairungruang et al., 2012; Yue et al., 2018). Several anisotropic models account for a dynamic modulus in their kinematic hardening law to improve springback simulation predictions (Wagoner et al., 2013).

Though these anisotropic models can capture deformation response and springback that occur during and after forming, when correctly calibrated to reflect a particular material and deformation path, they do not accurately capture the effects of strain path changes on nonlinear unloading response if backstress is not incorporated into the hardening law. In a prior study, Yue et al. (2018) reported a springback prediction error of approximately 17.5% for an 11% uniaxial pre-strain. Liao et al. (2020) performed twist springback simulations after applying uniaxial pre-strain and found that their simulations had an error of 15% and 12% in the rolling (RD) and transverse (TD) directions, respectively. In a similar study performed by Chen et al. (2021), errors of 28.6% and 14.6% along the RD and the TD directions were observed due to an overestimation of elastic modulus values in the model.

In this paper, EPSC model with a phenomenological backstress approach, along with a strain path sensitive dislocation density-based hardening law is used to predict springback in AA6016-T4 sheet material that is pre-strained along different strain paths and then subjected to various pure bending operations. It builds upon EPSC models that have been shown to accurately predict the microstructural and mechanical response to strain path changes, including non-linear unloading, residual stress fields, the Bauschinger effect, hardening rates, and texture of the material (Feng et al., 2020; Neil et al., 2010; Wollmershauser et al., 2012; Zecevic and Knezevic, 2019; Zecevic et al., 2016). A similar EPSC model has also been successful in predicting reverse and simple loading deformation in AA6022-T4 (Barrett and Knezevic, 2019), as well as multi-strain path deformation in AA6016-T4 (Sharma et al., 2022).

The use of AA6xxx series aluminum sheet metal has increased across the automotive industry because of a favorable combination of properties, including low density, high strength, and modest to very good levels of formability, depending on forming temperature. 6xxx series alloys, and specifically AA6016-T4, are precipitation-hardened with Al-Mg-Si composition. These alloys experience varying mechanical properties based on heat treatment, which affects the size and distribution of precipitates (Sato et al., 2002). The presence of precipitates contributes to the hardening behavior of the alloy by opposing applied stress necessary for dislocation slip through a mechanism known as Orowan looping. The formation and impact of these Orowan loops changes as the shape and size of the precipitates vary (Hu and Curtin, 2021; Kuwabara et al., 2017). This hardening mechanism is a key advantage of the 6xxx series alloys. They can be formed at room temperature in the T4 condition, and then strengthened during subsequent post-processing, such as paintbaking in automotive assembly operations, if needed.

Of particular interest in industrial fabrication is the prediction of springback in these sheet materials after a forming operation. Springback is a significant issue in forming of aluminum alloys, primarily because of how difficult it is to accurately predict the elastic recovery and subsequent change in part geometry needed to correctly assemble autobody components or subcomponents. Therefore, numerous studies have been conducted to understand the parameters and conditions that affect the springback of aluminum sheet materials (Cinar et al., 2021). The most commonly used bending operation is v-bending due to its simple tooling geometry, large range of bending angle capabilities, and economical set-up times (Abdullah and Samad, 2013; Abdullah et al., 2012; Adnan et al., 2017).

While the occurrence of springback behavior is well known and documented during various forming operations, there is a less common phenomenon known as springforward. Springback is known for the final part geometry having a larger bend angle than intended, while springforward or spring-go behavior produces a smaller bend angle geometry. This phenomenon has been documented through a limited number of studies and has been found to occur under specific conditions, including the use of a small punch tip radius to bottom bend thin sheet material (Bakhshivash et al., 2016; Grizelj et al., 2010; Thipprakmas and Rojananan, 2008). It is commonly understood that pure bending of material, like that commonly observed in v-bending, causes the fibers of the material to experience varying stresses and strains through the thickness of the sheet. The fibers of material that are closest to the point of contact with the punch tip experience compressive forces, while the fibers closest to the die experience tensile forces. The distribution of these stresses before unloading has a direct impact on the amount and the direction of the elastic unloading behavior (Zhang and Hu, 1998). In a study performed by Thipprakmas et al, the springback and spring-go behavior of an AA1100 sheet alloy utilizing v-die bending was investigated (Thipprakmas and Rojananan, 2008). The results showed that when all parameters are held constant, a larger punch tip radius produced the opposite stress distribution compared to conventional bending. Larger compressive stresses on the outside surface and larger tensile stresses on the inside surface of the specimen were observed, thus resulting in movement toward a smaller angle after release. These observed stresses were located away from the vertex of the bend, and dominated the stresses distributed beneath the punch tip. This phenomenon of springforward is also analyzed and reported on in the current study.

2. Experimental methods and modeling approach

Bending and springback experiments were carried out on a 100-ton Accurpress press-brake, using standard tooling. Fig. 1 shows the tooling geometries for the punch and die sets used to perform the bending experiments. Initial trials were performed on unstrained AA6016-T4 sheets, with the bend axis perpendicular to the rolling direction (RD), the transverse direction (TD) and 45° to the RD. All experiments were performed on specimens with the same geometry, having dimensions of $63.5 \text{ mm} \times 63.5 \text{ mm}$. Subsequent experiments were then performed on specimens that were pre-strained to varying amounts of effective strain (6%, 15%, 20%) relative to the RD direction. Pre-strains were applied in uniaxial tension, plane-strain tension, and biaxial tension, then the 63.5 m \times 63.5 mm specimens were cut from the pre-strained sheets via waterjet. All pre-strained specimens were oriented such that the RD direction was perpendicular to the v-die axis; in other words, the plastic strain induced by the bending experiment was applied along the RD of the sheet. Prior to performing a bend experiment, mineral oil was applied to the specimen, as well as to the punch and die set, to minimize friction. To measure springback, each specimen was tracked via highcontrast HDR video at the end of the punch stroke, then after unloading. Thickness measurements were taken after each experiment over five points along the specimen and compared to the unstrained material to ensure no thinning (coining) occurred at the bottom of the punch stroke.

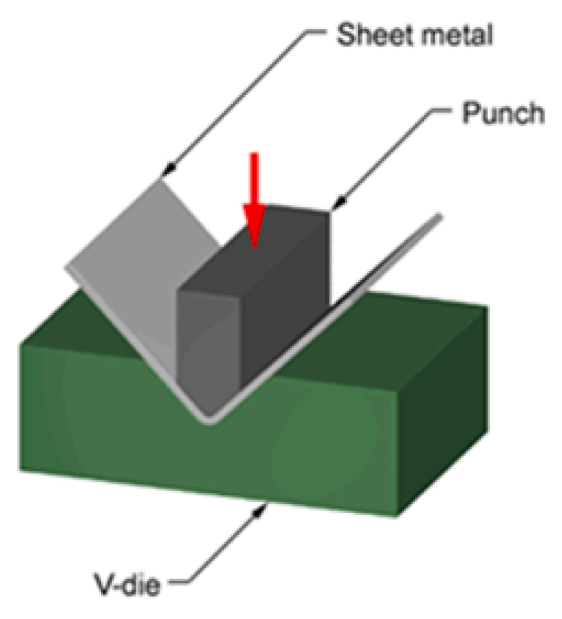


Fig. 1. Bottom bending tooling for springback experiments. The punch tip had a radius of 0.8 mm and the bend angle applied by the tooling at the bottom of the stroke was 88°. Springforward / springback angles were measured after removing the punch load.

2.1. Pre-Straining Methods: Biaxial Tension, plane strain Tension, and uniaxial tension

The biaxial and plane-strain tension tests were guided by a previous study on DP 600 steel sheets by Cheng et. al (Cheng et al., 2017). Forming limits for biaxial tension and plane-strain tension (with the major strain axis oriented along the RD) were measured using an Interlaken hydraulic press with standard Marciniak tooling. The tooling incorporates a 100 mm diameter punch with a flat top, making specimen extraction from the pre-strained material convenient for further testing. Deformation with Marciniak tooling includes the use of a carrier blank, made of the same material as the sheet being deformed, designed to limit the strain localization along the rim of the punch, so that a maximum strain level can be produced across the punch face. All experiments were performed with a clamp load of 200kN, using 0.5 mm thick Teflon sheets positioned between the sheet and punch, and mineral oil applied on the punch, Teflon sheet, carrier blank, and sheet specimen. While biaxial specimens were fully clamped, plane-strain tension required some experimentation to find the appropriate specimen width that imposed a plane-strain deformation path. The surface strains on each specimen were measured using Aramis digital image correlation (DIC) equipment

Specimen

Carrier
Blank

Punch

Bottom
Die

attached to the press. The Marcinak tooling and an example of a biaxial pre-strained specimen are shown in Fig. 2. Note that for the uniaxial pre-strains, a large tensile specimen was employed, with dimensions of 64 mm \times 635 mm. Following pre-straining, to effective strain levels of 6%, 15%, and 18–20% effective strain, bend specimens were carefully removed from the center of each pre-strained sheet using a shear.

Springback measurements were taken optically and analyzed using a 3-D profile tracing software on a VHX Keyence Digital Microscope (Fig. 3). The sheet profiles were measured and compared against the 88° die angle to compute springback angles in the sheet, after unloading. The software takes images from the bottom up to capture the profile of the material. Tools within the software allowed for measuring the angle of the profile generated from the photos taken by the microscope. Three sections of each sample were selected (Fig. 3b) and used to produce a 2-D generated side-view of the specimen where height and internal bend angle measurements were taken (Fig. 3c). Specimens with included angles of less than 88° after unloading have undergone "springforward", while specimens with angles of>88° are considered to have undergone "springback".

2.2. Material characterization

The composition of the 1 mm thick AA6016-T4 alloy sheets used for the experimental work is shown in Table 1. Stress–strain curves produced by uniaxial tension tests provided material properties necessary for initial characterization. Specimens were cut from the sheet along the rolling direction (RD), transverse direction (TD), and 45° to the RD of the sheet according to the ASTM E8 specification. The specimens were pulled at a 1.5 mm/min crosshead displacement rate and the force-strain data were recorded using load cell and extensometer output. Table 2 shows minor differences in the deformation response for the three orientations. The failure strain measured for each orientation ranged from 0.245 to 0.270, with RD exhibiting the greatest.

The unstrained base material texture was measured using EBSD to calibrate the model for the AA 6016-T4 alloy. Specimens strained to different levels of pre-strain in uniaxial, plane-strain, and biaxial tension were also evaluated for texture evolution and geometrically necessary dislocation (GND) content as a function of strain, to compare against the dislocation density calculated by the model; in this case statistically store dislocations (SSD), to be described later. High resolution EBSD (HREBSD) was employed to compute the GND density in the base material and the strained specimens, using OPENXY (Ruggles and Fullwood, 2015). A small sample sectioned from the gauge length of the prestrained specimens was prepared for microstructure analysis. The microscopy samples were removed using a diamond blade cutter, to avoid deformation of the material, and mounted in epoxy resin to be polished for EBSD scanning. The ND surface of the samples was first ground with grits of 400, 600, 800, 1200, and 1200 fine abrasive paper. The ground

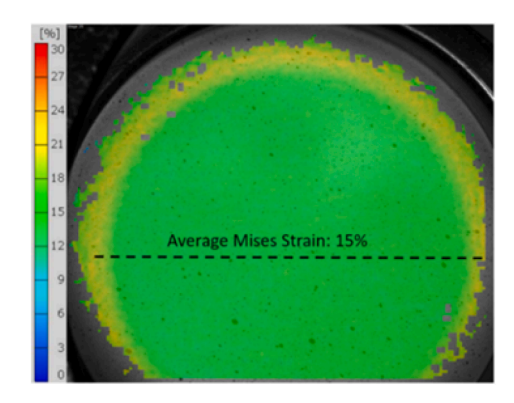


Fig. 2. (a) Marciniak tooling for biaxial and plane-strain tension pre-strain experiments, and (b) DIC strain map for a 15% pre-strained biaxial-tension specimen. Coupons for bend testing with 63.5 mm \times 63.5 mm dimensions were cut from the center of the flat portion of the Marcinak specimen, after applying different levels of pre-strain.

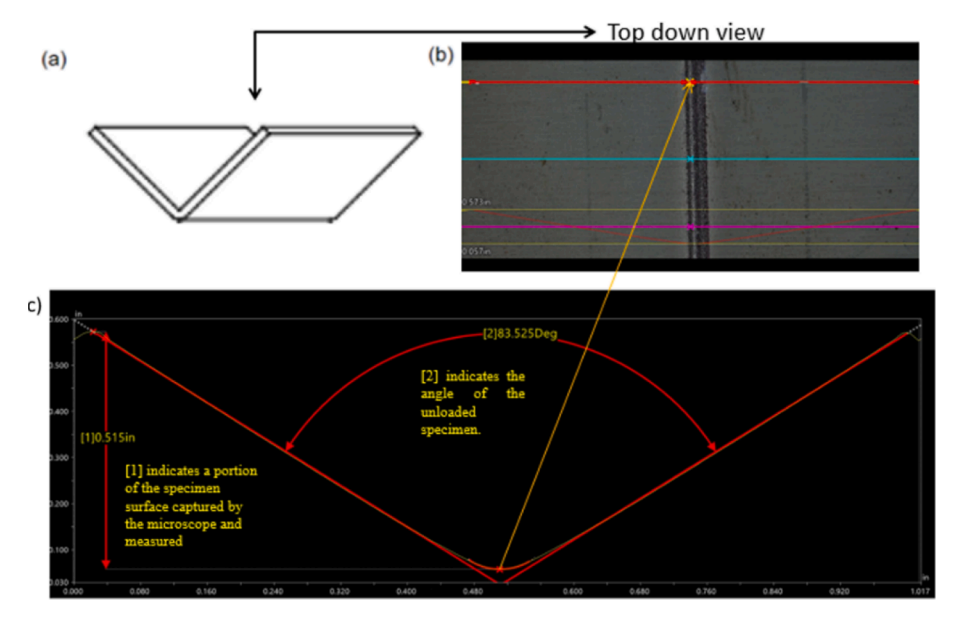


Fig. 3. Images of specimen after bending (a) are taken to produce a top-down view (b), which is used to produce 2-D bend profiles (c).

Table 1Nominal chemical composition of AA6016-T4.

Al	Si	Mg	Fe	Mn	Zn	Cu	Ti	Cr
96.4–98.8	1.0-1.5	0.25-0.6	0-0.5	0-0.2	0-0.2	0-0.2	0-0.15	0-0.1

Table 2Tensile properties of AA6016-T4 (strain values are true/natural and stress values are engineering/nominal).

Orientation	Young's modulus (GPa)	Failure strain	Yield strength (MPa)	Ultimate tensile strength (GPa)
RD	70.5	0.270	142	344
45° to RD	70.8	0.245	140	321
TD	71.7	0.249	140	326

samples were then electropolished using an electrolyte solution of 1:9 ratio of perchloric acid and methanol under 20 V and 2 amps at room temperature for 30 s. The polished samples were milled in an inert argon gas environment by a JEOL ion-beam cross-section polisher to remove the initial strain layer induced by polishing. The surface was first coarsely milled at 5 kV and 4.2 atm for 20 mins. A second finer step removed unevenness by milling the surface at 4 kV and 6.2 atm for 5 mins. The polished surface of the samples was scanned using EDAX OIM software ("OIM 6.0," 2010), and patterns were saved for evaluation using HREBSD. Three different areas of 120x120 microns with 70 nm step size were scanned for GND content on each specimen, where an example of one scan is shown in Fig. 4.

The GND calculations from the HREBSD scan data are based on the dislocation density tensor (α) by Nye:

$$\rho \approx \frac{1}{h} \|\alpha\|_{1}, \alpha = \nabla \times \beta \tag{1}$$

where ρ denotes dislocation density, b average Burger's vector, $\mathbf{\beta}$ elastic distortion as measured by HREBSD, and $||\mathbf{\alpha}||_1$ is the L_1 norm on a tensor.

2.3. EPSC simulation of Pre-Straining, Bending, and springback

Simulations of pre-straining, bending, and springback were per-

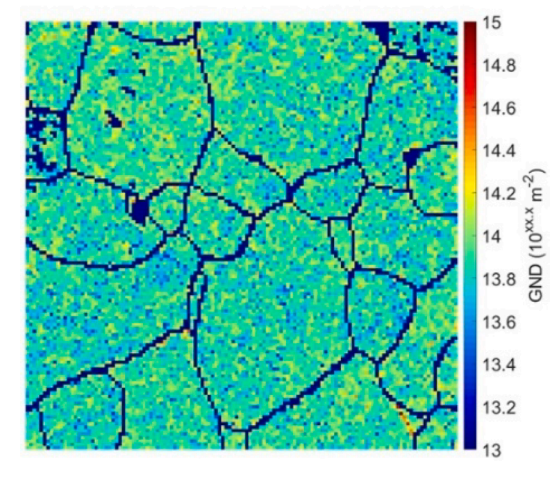


Fig. 4. GND content for unstrained AA 6016-T4, produced by HREBSD (Sharma et al., 2022).

formed using an EPSC polycrystal plasticity model that was developed by Zecevic and Knezevic (Zecevic and Knezevic, 2019) and has been used to model plastic deformation under different strain paths and for cyclic loading in prior work in AA 6016-T4 (Daroju et al., 2022; Feng et al., 2021a; Feng et al., 2021b; Sharma et al., 2022). In the brief description that follows, the subscript FE indicates variables returned or passed from the Abaqus FEM engine to the UMAT subroutine. Every material point of the FE mesh considers a set of weighted crystal orientations representing a polycrystalline aggregate. The EPSC material model calculates Cauchy stress at the end of each strain increment, $\sigma_{FE}^{t+\Delta t}$, for a strain increment, $\sigma_{FE}^{t+\Delta t}$, given by Abaqus. The strain increment is based on the boundary conditions applied to the mesh. The strain accommodated by EPSC at each material point is updated according to:

$$\varepsilon_{FE}^{t+\Delta t} = \varepsilon_{FE}^{t} + \Delta \varepsilon_{FE} \tag{2}$$

The implicit coupling of the EPSC model and FEM requires a Jacobian matrix, $\frac{\partial \Delta \sigma_{EE}}{\partial \Delta e_{FE}}$, for calculating subsequent displacement fields in arriving at the solution. The Jacobian is (Feng et al., 2022; Zecevic and Knezevic, 2019):

$$\frac{\partial \Delta \sigma_{FE}}{\partial \Delta \varepsilon_{FE}} = \frac{\partial \left(\sigma_{FE}^{t+\Delta t} - \sigma_{FE}'\right)}{\partial \Delta \varepsilon_{FE}} = \frac{\partial \Delta \bar{\sigma}}{\partial \Delta \bar{\varepsilon}} = \frac{\partial \left(\bar{\mathbf{L}}^{inc} \Delta \bar{\varepsilon}\right)}{\partial \Delta \bar{\varepsilon}} = \bar{\mathbf{L}}^{inc}$$
(3)

where $\bar{\mathbf{L}}^{inc}$ is the stiffness from the Cauchy stress and strain increments (Zecevic and Knezevic, 2019). Details of the EPSC model and associated hardening law are provided in the Appendix A.

The backstress component of hardening is based on a phenomenological formulation to influence unloading and the Bauschinger effect. The evolution of backstress per slip system, τ_{bs}^s , is a function of shearing strain on slip systems, γ^s . The laws for $d\gamma^{s^+} > 0$ and $\tau_{bs}^{s^+} > 0$ are:

$$\tau_{bs}^{s^{+}} = \tau_{bs}^{sat} (1 - \exp(-\nu \gamma^{s^{+}})) \tag{4}$$

$$\tau_{bc}^{s^-} = -A\tau_{bc}^{s^+} \tag{5}$$

where au_{bs}^{sat} is a saturation value of the backstress, A is a parameter for asymmetric evolution of the backstress on a slip system in two opposite directions s+ and s-, γ_b and ν are material fitting parameters. The shear strain γ^s is recorded from the point $au_{bs}^{s^+}=0$. The laws for $d\gamma^{s^+}>0$ and $au_{bs}^{s^+}<0$ are:

$$\tau_{bs}^{s^+} = -(A+1)\tau_{bs}^{sat} \exp\left(-\frac{\gamma^{s^-}}{\gamma_b}\right) + \tau_{bs}^{sat}$$
 (6)

$$\tau_{bs}^{s^{-}} = -\frac{1}{4}\tau_{bs}^{s^{+}} \tag{7}$$

where the shear strain γ^{-} is recorded from the point of local road reversal. The backstress changes the activation of slip systems as:

$$\sigma^c \bullet \mathbf{m}^s - \tau^s_{bs} = \tau^s_c \tag{8}$$

$$\widehat{\boldsymbol{\sigma}}^c \bullet \mathbf{m}^s - \dot{\boldsymbol{\tau}}_{bs}^s = \dot{\boldsymbol{\tau}}_c^s \tag{9}$$

while the backstress evolves with shearing rates using:

$$\dot{\tau}_{bs}^{s} = \sum_{i} h_{bs}^{ss} \dot{\gamma}^{s} \tag{10}$$

where h_{ss}^{ss} is the backstress matrix. The selected law is as follows (Zecevic and Knezevic, 2019):

$$\tau_{bs}^{s} = \mathbf{m}^{s} \bullet \sigma_{bs}^{c} = \tau_{bs,sys}^{s} + 2 \sum_{s} \mathbf{m}^{s} \bullet \mathbf{m}^{s} \tau_{bs,sys}^{s}^{s}, \tag{11}$$

where

$$\tau_{bs,sys^*}^{s'} = \begin{cases} \tau_{bs,sys}^{s} & \text{if } \tau_{bs,sys}^{s} > 0\\ 0 & \text{if } \tau_{bs,sys}^{s} < 0 \end{cases}$$
 (12)

In Eq. (11), σ_{bs}^c is the back-stress tensor based on the contribution from the slip system level sources over s when $s \neq s$. The slip system level back-stress is:

(if $d\gamma^{s^+} > 0$ and $\tau^{s^+}_{bs,sys} > 0$):

$$\tau_{bs,svs}^{s^{+}} = \tau_{bs}^{sat} (1 - exp(-\nu \gamma^{s^{+}}))$$
(13)

$$\tau_{bs,sys}^{s^-} = -A\tau_{bs,sys}^{s^+} \tag{14}$$

(if $d\gamma^{s^+}>0$ and $au^{s^+}_{bs,sys}<0$)

$$\tau_{bs,sys}^{s^+} = -(A+1)\tau_{bs}^{sat} exp\left(-\frac{\gamma^{s^-}}{\gamma_L}\right) + \tau_{bs}^{sat}$$
(15)

$$\tau_{bs,sys}^{s^{-}} = -\frac{1}{A}\tau_{bs,sys}^{s^{+}} \tag{16}$$

The fitting constants for the backstress law are a saturation value, τ_{bs}^{sat} , a parameter governing an asymmetric evolution in s+ and s-, A, the denominator, γ_b , and a multiplier, ν . The shearing strain, γ^s , is a value at the load reversal.

Model parameters for the hardening and backstress laws were calibrated through tensile tests and HREBSD scan data, performed in prior work (Sharma et al., 2022) on the AA 6016-T4 material. The following parameters associated with the hardening laws were fit: initial slip resistance, τ_0 , trapping rate coefficient, k_1 , activation barrier for depinning, g, and drag stress, D. The fitting procedure started with varying τ_0 to fit yield stress. Next, k_1 , was adjusted such that the initial hardening slope is reproduced. Finally, g and D were adjusted to match the hardening behavior. The latent hardening parameters reproduced the anisotropy. In order to capture the strain path changes and underlying load reversals, the following back-stress law parameters were fit: saturation value for back-stresses τ_{bs}^{sat} , asymmetry factor, A, and parameters ν and γ_b . The same parameters, used in the present study, are shown in Tables 3-5 below.

Most EPSC simulations of pre-strain and bending in the current work were performed with the slip system backstress component included in the hardening law; however, modeling without backstress was also performed in order to assess its relative influence on model accuracy. In addition, some J_2 plasticity simulations were run with Abaqus standard (the latter was only used for unstrained base material bending and springback simulations) for comparison with the EPSC crystal plasticity approach. For cases where a pre-strain was imparted to the sheet, the correct boundary conditions were applied in order to reach various effective strain levels, for each desired pre-strain path, as shown in Fig. 5.

The pre-strain simulation results were compared to experimentally measured pre-strains (using the DIC approach shown in Fig. 2) for validation, as shown in Fig. 6.

After pre-strains were applied in the first simulation step, the bending/springback simulation was performed using the model tooling shown in Fig. 7, where the sheet mesh had 1872 C3D20R elements, including 5 elements through the thickness. The tooling was considered rigid and isothermal for the purpose of these room temperature simulations.

3. Results and discussion

3.1. Bending and springback of as-received material

The texture data generated by electron backscatter diffraction (EBSD) for the EPSC model contained approximately 1000 grains that were subsequently compacted to 100 grains for each orientation (Barrett et al., 2019; Eghtesad et al., 2018; Knezevic and Landry, 2015). The compaction is a necessary step to decrease computation time; as can be seen in Fig. 8, there is no difference between the original and the compacted pole figures, for the unstrained base material (100% accurate to $L=16\ GSH\ expansion$).

Initial EPSC simulations of bending and subsequent springforward on unstrained base material were performed using different elements within Abaqus, including the CPE4, CPE8, and CPE8R elements. The CPE8R element was the most accurate, so this choice was retained for a comparison with the experiments, as shown in Fig. 9.

For the experiments and simulations on the unstrained base material,

Table 3
Latent hardening parameters.

a_0	a_1	a_2	a_3	a_4	a_5
0.068	0.068	0.0454	0.625	0.137	0.122

Table 4Fitting parameters used for the evolution of slip resistance.

$ au_0[ext{MPa}]$	$k_1[m^{-1}]$	g	D[MPa]	$\rho_{0,for}^s \big[m^{-2} \big]$
25	1.38×10^8	0.09	400	4.1e12

Table 5Fitting parameters used for the evolution of slip system backstress.

$ au_{bs}^{sat}[ext{MPa}]$	ν	γ_b	Α
5	560	0.001	1

all angles after unloading were less than the die angle of 88, characteristic of the springforward phenomenon. Because thin sheet material

(1 mm thickness) was used for the experiments, and because the punch tip radius was small (0.8 mm), this behavior was anticipated based on the results of prior studies, discussed earlier in the paper. A comparison of standard J2 plasticity predictions with the EPSC crystal plasticity results is shown in Table 6 and Fig. 10.

While the J2 isotropic modeling approach captured the general springforward phenomenon after bending, it overestimated the amount of springforward, or included angle contraction, in each case. This result agrees with prior work, where overestimation of the springback/springforward effect in aluminum alloys was observed for isotropic modeling approaches that do not account for Bauschinger effect and associated backstresses (Li et al., 2002). The predicted values from the J2 isotropic model differed with experiment by as much as 2.4% (2.0°), for the 45° to RD specimen. By contrast, the EPSC predictions were close to the experimental values; at worst, within 0.4% (0.3°, TD specimen),

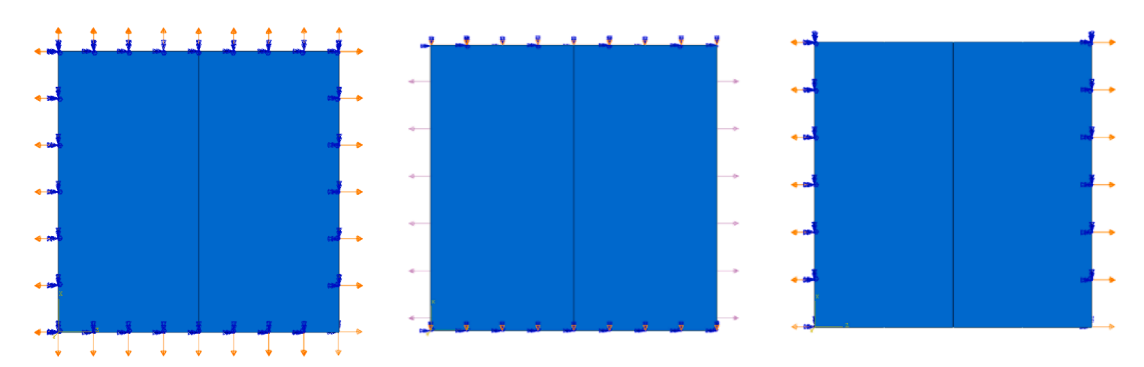


Fig. 5. Pre-strain simulations imparted various levels of effective strain to sheet blanks prior to the bending/springback step. Boundary conditions are shown for pre-strain simulations in (a) biaxial tension, (b) plane-strain tension, and (c) uniaxial tension.

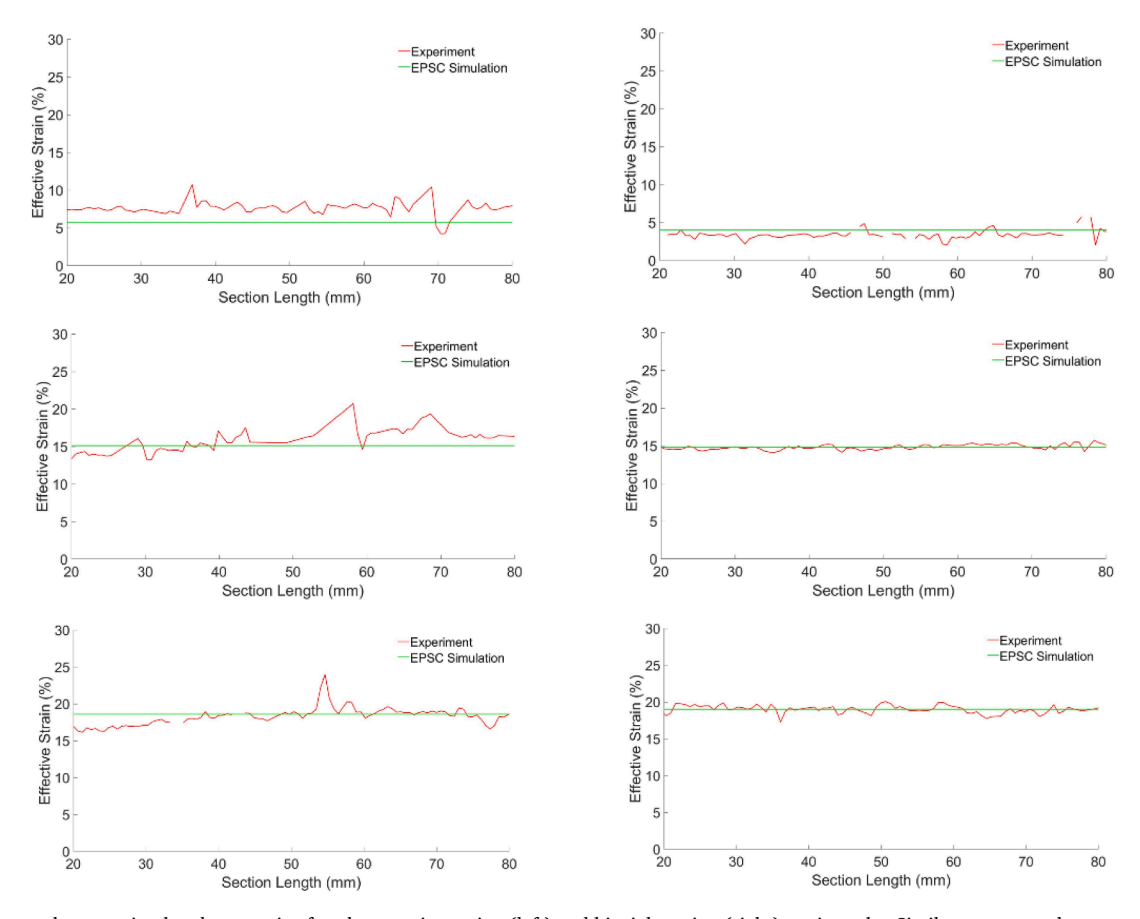


Fig. 6. Experimental versus simulated pre-strains for plane-strain tension (left) and biaxial tension (right) strain paths. Similar agreement between experiment and simulation was obtained for uniaxial tension pre-strains.

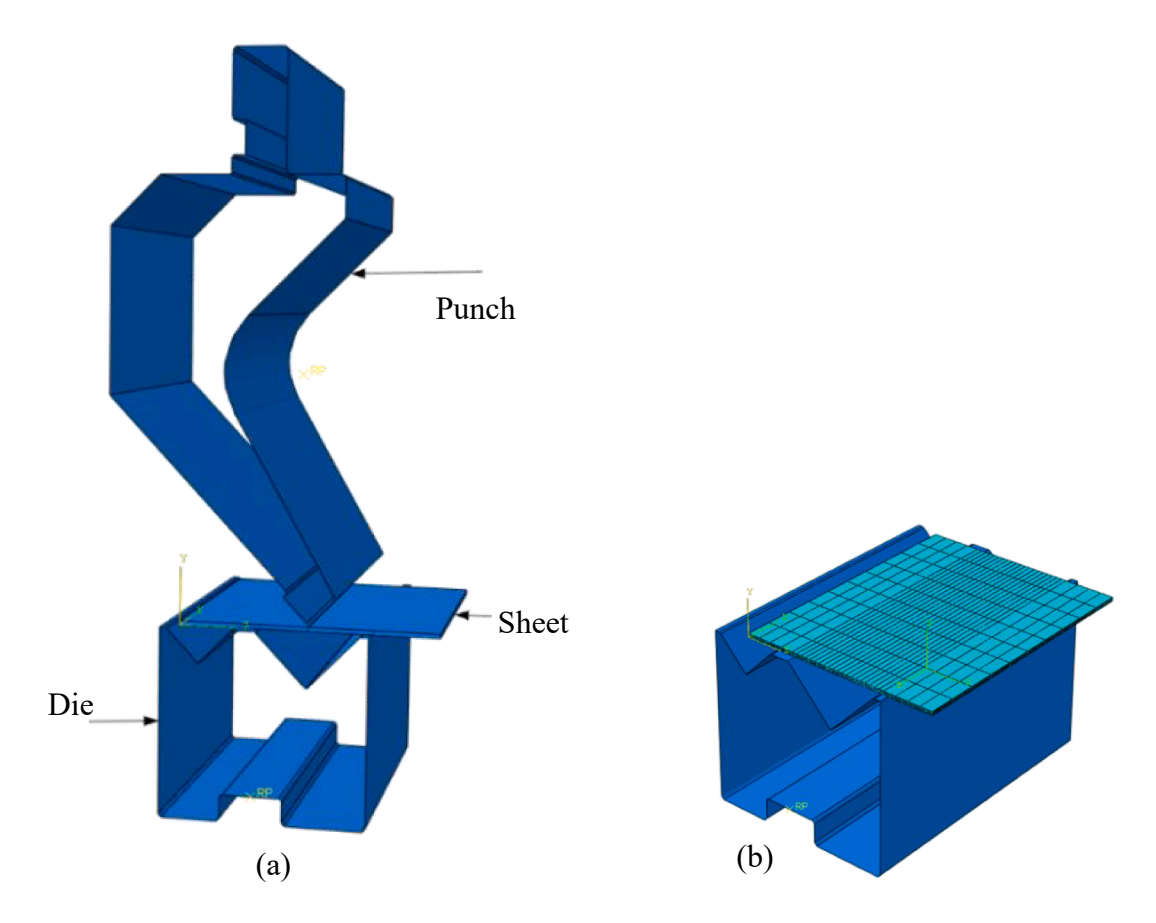


Fig. 7. (a) Bending model where the punch and die were both considered rigid for the purpose of the simulation. The punch/die bend angle was 88 and the punch radius was 0.8 mm; (b) the sheet mesh, shown resting on the die, consisted of 1872 C3D20R elements, with 5 elements through the thickness.

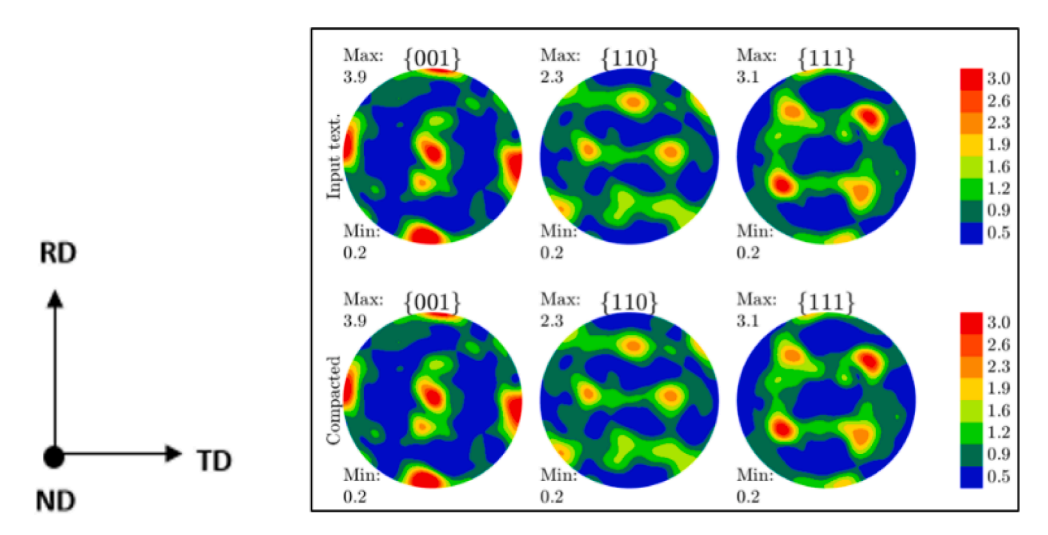


Fig. 8. Original texture for AA6016-T4 comprising ~1000 grains (top), and texture data compacted to 100 grains (bottom) for EPSC simulations.

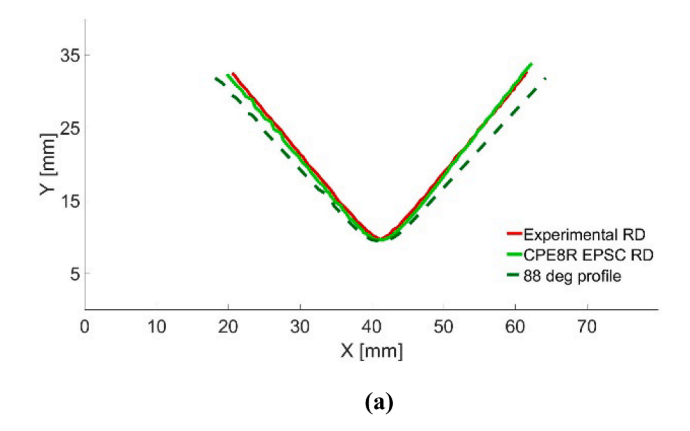
highlighting the need for modeling backstress development as a function of plastic strain in order to accurately calculate part shape after unloading. Percent error terms were calculated with respect to the included angle of the specimen, after unloading.

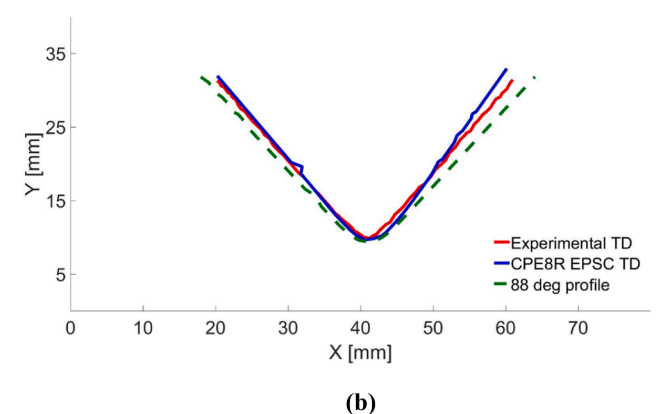
3.2. Bending and springback after pre-straining in uniaxial, plane-strain, and biaxial tension

Given the superior accuracy of the EPSC model for the unstrained

base material predictions, further work was done comparing EPSC results with experiments when pre-strain was first applied to the sheets. Data from HREBSD scans on pre-strained material included dislocation densities (GND) that were used to calibrate the backstress component of the hardening law in the EPSC model, as described in (Daroju et al., 2022; Sharma et al., 2022). Table 7 shows the effective pre-strain levels for each deformation type (strain-path), as well as the subsequent springforward/springback angle after bending.

Even with the change in strain path, where a pre-strain step was





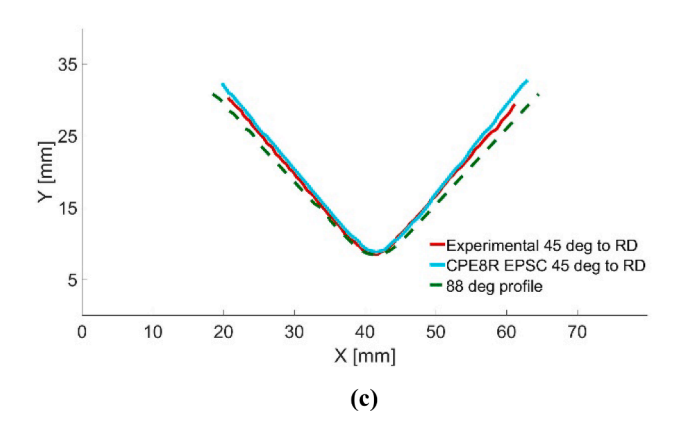


Fig. 9. Experimental versus EPSC simulated specimen profiles after springback for base material sheet for (a) RD, (b) TD, and (c) 45° to RD oriented perpendicular to bend axis. Both the experiment and the predicted included angles are less than 88° after unloading, indicating a springforward motion.

 $\begin{tabular}{lll} \textbf{Table 6} \\ \textbf{Comparison of J2 plasticity isotropic model and EPSC predictions against experiment.} \end{tabular}$

Orientation	Experimental Springforward Angle (°)	Isotropic Model Springforward Angle (°)	EPSC Model Springforward Angle (°)
RD	83.7	82.9	83.8
TD	83.8	82.4	84.1
45° to RD	83.9	81.9	84.1

followed by a bending/unloading step, the EPSC predictions typically only deviated from experiment by 0.2-1.7%, with a maximum error of 3% (2.8°) in the case of 18.5% pre-strain in biaxial tension. The relatively small differences appear to be reasonable, and most likely within

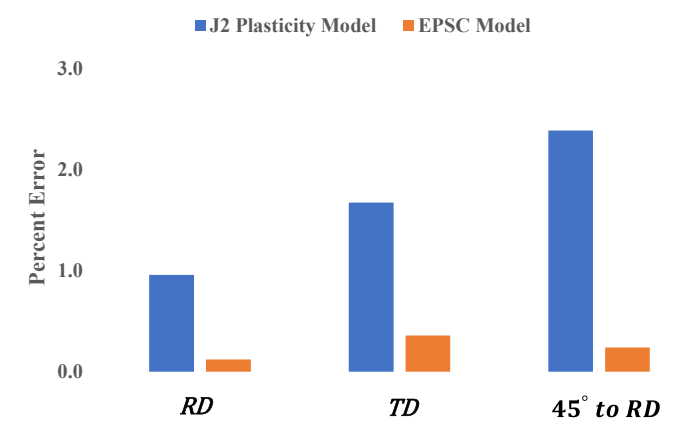


Fig. 10. Percent error of J2 and EPSC model predictions of springforward angle, with respect to experiment.

Table 7Springforward/Springback angles as a function of pre-strain level, for each strain path.

Strain path	Effective pre-strain (%)	Experimental Measurement (°)	EPSC Prediction (°)	Difference (°)
Uniaxial	6	84.6	85.7	1.1
Tension	15	87.0	87.2	0.2
	21	89.7	90.2	0.5
Plane-	5.5	84.1	85.5	1.4
strain	15.2	87.0	87.2	0.2
Tension	19.4	87.9	89	1.1
Biaxial	6.4	83.8	85	1.2
Tension	14.7	89.5	90	0.5
	18.5	94	91.2	-2.8

tolerance when considering manufacturing assembly requirements. Importantly, both springforward (included angle less than 88) and springback (included angle > 88) trends are predicted correctly. The correlation between model results and experimentally measured angles for all pre-strain modes and levels (from Table 7) is shown in Fig. 11, with a 91% correlation.

Springforward/springback angles were also plotted as a function of effective pre-strain levels in Fig. 12 for each strain path, where the effect of backstress in the EPSC prediction is evaluated. It is seen that model results with backstress are slightly greater than the experimental measurements for uniaxial tension and plane strain tension, as pre-strains increase from $\sim 6-20\%$, but the trendlines fit through the data are nearly parallel with respect to experiment for uniaxial and plane-strain tension pre-strain, and somewhat less so for the biaxial tension case.

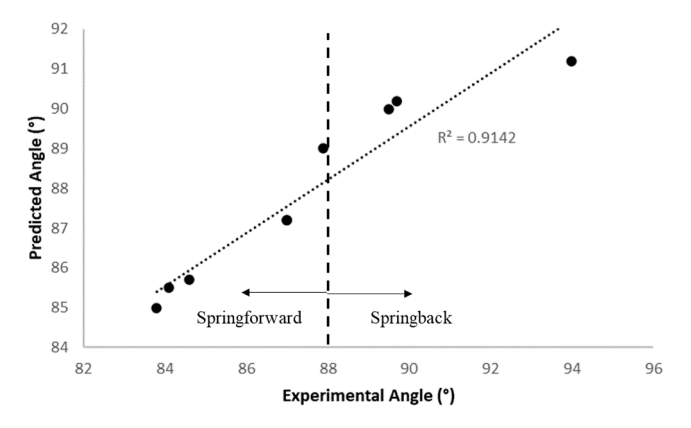
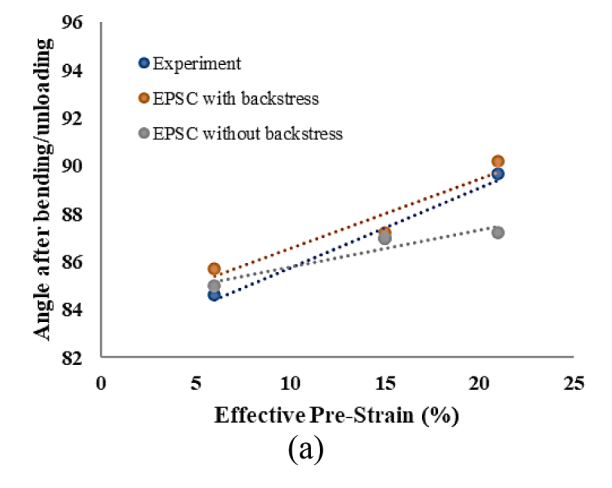


Fig. 11. Correlation between model predictions and experiments, for all prestrain paths (uniaxial, plane-strain, biaxial) and levels (6%, 15%, and 20%).



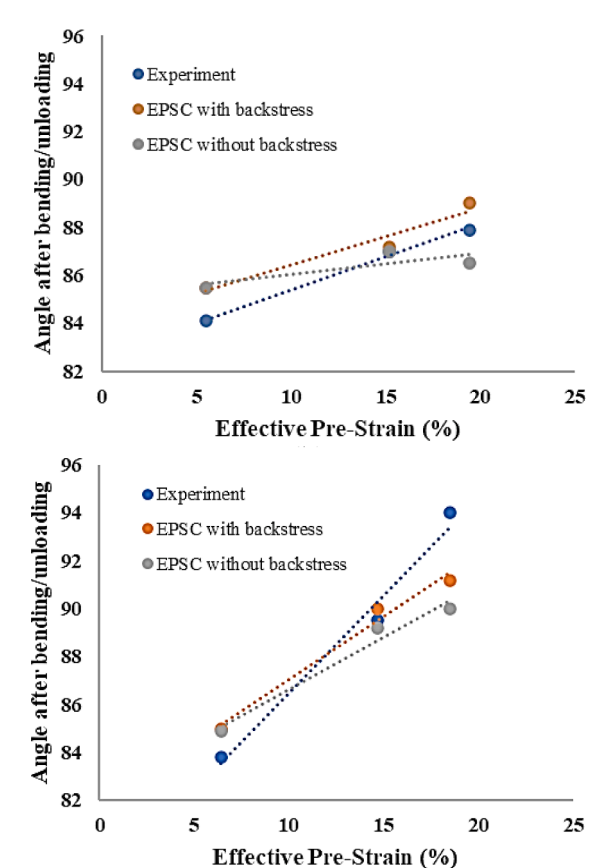


Fig. 12. Springforward/springback angles for specimens pre-strained in (a) uniaxial tension, (b) plane-strain tension, and (c) biaxial tension. Predictions with backstress and without backstress are compared to experiments.

(c)

However, when backstress is not included in the model, angle predictions diverge significantly from the experiment for all three pre-strain cases

EPSC simulations without backstress do not accurately capture the relationship between pre-strain type/level and springback angle after bending, especially in the case of uniaxial tension and plane strain tension. In these last cases, the transition from springforward to springback is not predicted without backstress, i.e. predicted specimen angles are less than 88 (springforward) and do not exceed 88 (springback) at higher pre-strain levels, as seen in the experiment. When backstress is included in the model hardening law, the springforward to

springback transition is predicted reasonably well.

While there is little prior work on the effect of different pre-strains on subsequent bending/springback performance in Al alloys, one study did apply uniaxial pre-strains prior to bending/springback to an extra deep drawing quality (EDDQ) sheet steel (Joo et al., 2023). In this case, a crystal plasticity modeling approach was able to predict springback angles after pre-strains of 0, 6, and 15%. The backstress development in the steel was modeled in similar fashion to the current approach, where the CRSS of each slip system was a function of forest dislocation density plus a backstress term, scaling with accumulated shear, which acts to reduce the resolved shear stress needed to move dislocations. It was seen that springback increased with greater pre-strain levels, as was seen in the current work on AA 6016-T4, confirming that higher levels of backstress promote greater springback, owing to the movement of reversible dislocations during unloading.

The effect of backstress on EPSC model accuracy is seen to be increasingly influential for greater levels of pre-strain, where the slopes of the curves in Fig. 12 diverge for EPSC predictions with backstress versus EPSC predictions without backstress. There appears to be a correlation between SSD content predicted by the model at the end of each pre-strain step, and the influence of backstress on the prediction of specimen angle after bending/unloading. SSD content is seen in Fig. 13 for each strain path and each pre-strain level.

The apparent correlation between SSD content at the end of the prestrain step and the accuracy of springback angle prediction, when backstress is included, appears to be related to slip systems activated by each strain path. For the uniaxial pre-strain, the higher level of SSD content predicted by the model (Fig. 13) is achieved because there are fewer active slip systems, compared to plane-strain or biaxial tension, as reported recently in a study on an 8xxx series aluminum (Rakshit et al., 2022). Fewer slip systems to accommodate plastic deformation results in more concentrated dislocation density on each slip system, and thus results in more directional backstress development for a given level of effective strain.

Prior work in AA 6063-T6 revealed that backstresses increased with greater levels of plastic deformation (Muhammad et al., 2017), as observed in the present work. This relationship explains the divergence of EPSC simulation predictions for the cases where backstress is modeled, versus when it is not, as effective pre-strain levels were increased, especially for the uniaxial tension pre-strain case.

4. Summary and conclusions

Bending and springback experiments were performed on 1 mm thick

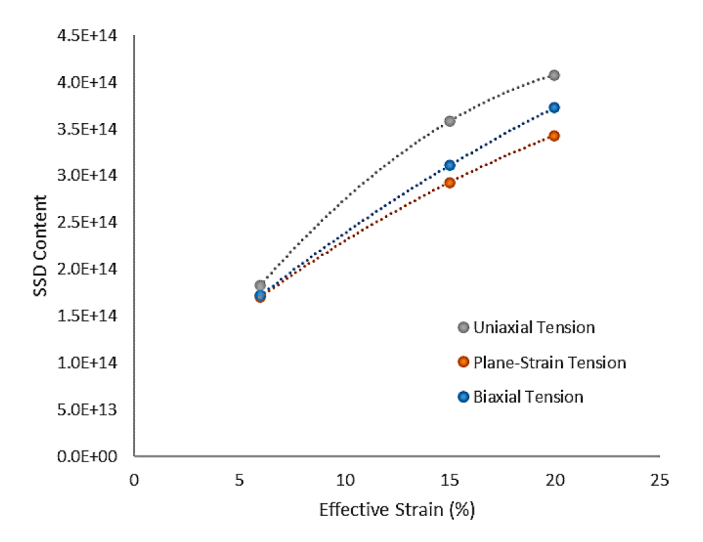


Fig. 13. SSD content provided by EPSC simulation for each strain path, for the 6%, 15%, and 20% effective pre-strain levels.

AA 6016-T4 sheets, where a punch formed the sheets into an 88 deg v-block die, then released the material, allowing it to springback. Careful measurements documented springback angles for the base material specimens oriented along the RD, TD, and 45 deg directions (bend axis perpendicular to each of these directions). Additional experiments were conducted where pre-strains were first imparted to the sheet specimens, using Marcinak tooling to apply plane-strain and biaxial pre-strains and a large tensile specimen to impart uniaxial tension pre-strains. Specimens cut from these pre-strained sheets were then used for bending/springback experiments. A crystal plasticity EPSC code with the ability to model the directional evolution of dislocation density and backstress during plastic deformation was employed to simulate the bending/springback experiments, for both the base material and for pre-strained specimens. The following conclusions can be drawn from the combined experimental and modeling results:

- 1. The base material bending/springback experiments all exhibited the springforward phenomenon, where the bend angle after unloading was less than the v-block die angle (88°).
- 2. When pre-strains were applied in uniaxial, plane-strain, and biaxial tension to effective strain levels of 6, 15, and 20%, specimens showed a transition from springforward to springback at higher pre-strain levels.
- 3. The EPSC model with backstress provided accurate predictions of experimental springforward angles in the base material, with an error of 0.4% (0.3°) in the worst case, while the isotropic model overpredicted springforward angles by as much as 2.4% (2°).
- 4. The EPSC model with backstress was accurate in predicting the transition from springforward (angle less than 88°) to springback

- (angle $> 88^\circ$), as a function of applied pre-strain, while the EPSC model without backstress was not predictive of the transition.
- 5. The effect of backstress in the model was increasingly influential on model accuracy for greater levels of pre-strain. This influence was especially true for the uniaxial pre-strain case and appears to be proportional to the rise in dislocation density (SSD) computed by the model during the pre-strain step, prior to bending. As such the backtress component of hardening is seen to be critical to accurate modeling of springback, especially in cases where strain path changes occur prior to unloading.

Declaration of Competing Interest

The authors declare that they have no known competing financial interests or personal relationships that could have appeared to influence the work reported in this paper.

Data availability

Data will be made available on request.

Acknowledgements

The work presented in this paper was supported by the National Science Foundation grant numbers CMMI-1926662 (BYU) and CMMI-1926677 (UNH). The AA 6016-T4 sheet material used for experiments was provided by Commonwealth Aluminum (Madison Heights, MI).

Appendix A

This appendix summarizes the FE-EPSC details, including the EPSC material model and hardening law for the evolution of slip resistance.

A.1 EPSC material model

A material model based on the EPSC theory was used in the present work to perform the simulations. The model is an implicit formulation of the EPSC model incorporated in the implicit FEM framework, termed FE-EPSC (Zecevic and Knezevic, 2019). The description that follows, uses \cdot and \otimes to denote dot and tensor products, respectively. A polycrystalline aggregate in EPSC is represented by a set of grains/inclusions. Every grain/inclusion is an elasto-plastic medium interacting with a homogeneous-equivalent-matrix (HEM). The inclusion has a distinct crystallography/orientation, ellipsoidal shape, and volume fraction. The crystal orientation and shape evolve with plastic strain.

The EPSC model relies is the following constitutive equation

$$\hat{\sigma} = \dot{\sigma} + \sigma \mathbf{W} - \mathbf{W}\sigma,\tag{1}$$

for calculating the Jaumann rate of Cauchy stress, $\hat{\sigma}$ (Nagtegaal and Veldpaus, 1984; Neil et al., 2010). The equation applies to a point, which can be a single crystal or a polycrystal. The other quantities in the equation, **W** and σ are the spin tensor and Cauchy stress tensor, respectively. The corresponding quantities at the crystal level are specified with the superscript c as \mathbf{W}^c and σ^c . The Jaumann rate of Cauchy stress at the crystal level is $\widehat{\sigma}^c$ is

$$\widehat{\sigma}^c = \mathbf{C}^c \left(\dot{\varepsilon}^c - \dot{\varepsilon}^{pl,c} \right) - \sigma^c tr(\dot{\varepsilon}^c),\tag{2}$$

where \mathbf{C}^c is the 4th rank crystal level elastic stiffness tensor, $\dot{\epsilon}^c$ is the crystal level strain rate, and $\dot{\epsilon}^{pl,c}$ is the plastic portion of the strain rate. The plastic portion of the strain rate is a sum of the products between the symmetric Schmid tensor, $\mathbf{m}^s = \frac{1}{2}(\mathbf{b}^s \otimes \mathbf{n}^s + \mathbf{n}^s \otimes \mathbf{b}^s)$ and shearing rates, $\dot{\gamma}^s$, over active slip systems, s, in grain, s, i.e. $\dot{\epsilon}^{pl,c} = \mathbf{m}^s \dot{\gamma}^s$. The Schmid tensors comprises the slip directions parallel to the Burgers vectors, \mathbf{b}^s , and the plane normals, \mathbf{n}^s .

The crystal and polycrystal stress and strain rate relations are also expressed as

$$\widehat{\sigma}^c = \mathbf{L}^c \widecheck{\varepsilon}^c,$$
 (3a)

$$\hat{\sigma} = \mathbf{L}\dot{\varepsilon},$$
 (3b)

where \mathbf{L}^c and \mathbf{L} are the elasto-plastic stiffness tensors at the crystal level and polycrystal level, while $\dot{\epsilon}$ is the total strain rate over the polycrystal. The former is derived from Eq. (2) and using a hardening law for the evolution of slip resistance, while the latter is evaluated using the self-consistent (SC) homogenization procedure (Eshelby, 1957; Lipinski and Berveiller, 1989; Neil et al., 2010; Turner and Tomé, 1994; Zecevic et al., 2015). The procedure starts from volume averages for stress and strain-rate as

$$\widehat{\sigma} = \langle \widehat{\sigma}^c \rangle$$
 and $\widehat{\varepsilon} = \langle \widehat{\varepsilon}^c \rangle$. (4)

Activation of slip systems is based on the two conditions

$$\sigma^c \bullet \mathbf{m}^s = t_c^s$$
, (5a)

$$\widehat{\sigma}^c \bullet \mathbf{m}^s = \widehat{\tau}^s$$
 (5b)

where, r_c^s is the slip resistance, which will be defined shortly. The first condition ensures that the stress is on the yield surface of crystals, while the second condition is the consistency condition ensuring that the stress remains on the surface of crystals (Knockaert et al., 2000; Zecevic et al., 2019). Crystal lattice reorientation is accounted for using the spin tensors

$$\mathbf{W}^c = \mathbf{W}^{c,app} - \mathbf{W}^{pl,c},\tag{6}$$

where $\mathbf{W}^{c,app}$ and $\mathbf{W}^{pl,c}$ are applied and plastic spin tensors. The latter is $\mathbf{W}^{pl,c} = \sum_s \dot{\gamma}^s \mathbf{q}^s$ with $\mathbf{q}^s = \frac{1}{2} (\mathbf{b}^s \otimes \mathbf{n}^s - \mathbf{n}^s \otimes \mathbf{b}^s)$.

A.2 Hardening law

Indices s + and s- refer to positive and negative directions of slip systems in the description below, while both positive and negative directions are denoted with s. α enumerates slip modes/families, which for the face centered cubic (FCC) AA6016-T4 is $\alpha = 1$, $\{111\}\langle 1\bar{1}0\rangle$. The hardening law used in the present work is formulated based on the evolution of dislocation densities (Beyerlein and Tomé, 2008; Knezevic et al., 2014). The law has been used in predicting the mechanical response and texture evolution of AA6016-T4 (Daroju et al., 2022) and AA6022-T4 (Ferreri et al., 2022; Zecevic and Knezevic, 2015; Zecevic and Knezevic, 2018).

The slip resistance is

$$\tau_c^s = \tau_0^a + \tau_{forest}^s + \tau_{debris}^a,\tag{7}$$

where τ_0^a is an initial value that does not evolve, τ_{forest}^s is a contribution from statistically stored dislocations, and τ_{debris}^a is a contribution from dislocations stored as debris. The latter two terms evolve with plastic strain. The forest term is (Knezevic et al., 2013b; Knezevic et al., 2012)

$$\tau_{forest}^{s} = b^{\alpha} \chi \mu^{\alpha} \sqrt{\sum_{s'} L^{s'} \rho_{tot}^{s'}}$$
 (8)

where $b^a = 2.8610^{-10}$ m is the Burgers vector for aluminum, $\chi = 0.9$ is a strength of dislocation interaction constant, ρ_{tot}^s is the total dislocation density of forest type for s^{th} slip system, and $L^{ss'}$ is a latent interaction matrix (Franciosi and Zaoui, 1982; Khadyko et al., 2016). Entries of the latent matrix are based on simulations presented in (Devince et al., 2006; Hoc et al., 2004).

The debris contributing term is (Knezevic et al., 2016; Knezevic et al., 2013c)

$$\tau_{debris}^{\alpha} = 0.086\mu^{a}b^{a}\sqrt{\rho_{deb}}\log\left(\frac{1}{b^{a}\sqrt{\rho_{deb}}}\right) \tag{9}$$

where ρ_{deb} is the dislocation density of debris type (Madec et al., 2003).

The total dislocation density is

$$\rho_{tot}^{s} = \rho_{for}^{s} + \rho_{rev}^{s} + \rho_{rev}^{s}, \tag{10}$$

where ρ_{for}^s is the forward on s, while $\rho_{rev}^{s^+}$ and $\rho_{rev}^{s^-}$ are the reversible dislocation densities on the s^+ and s^- positive/negative directions providing strain path sensitivity, respectively. Temperature and strain rate sensitive laws are implemented for evolution of these dislocation densities with shearing strains as (Khadyko et al., 2016; Kitayama et al., 2013; Kocks and Mecking, 1981)

$$(\text{If } d\gamma^{s^+} > 0)$$

$$\frac{\partial \rho_{for}^s}{\partial \gamma^s} = (1 - p)k_1^{\alpha} \sqrt{\sum_{s'} g^{ss'} \rho_{tot}^{s'}} - k_2^{\alpha}(\dot{\varepsilon}, T) \rho_{for}^s, \tag{11a}$$

$$\frac{\partial \rho_{rev}^{s^+}}{\partial \gamma^s} = p k_1^{\alpha} \sqrt{\sum_{s'} g^{ss'} \rho_{tot}^{s'}} - k_2^{\alpha}(\dot{\varepsilon}, T) \rho_{rev}^{s^+}, \tag{12a}$$

$$\frac{\partial \rho_{rev}^{s^-}}{\partial \gamma^s} = -k_1^{\alpha} \sqrt{\sum_{s} g^{ss} \rho_{tot}^{s'}} \left(\frac{\rho_{rev}^{s^-}}{\rho_0^s} \right)^m, \tag{13a}$$

 $(\text{If } d\gamma^{s^-} > 0)$

$$\frac{\partial \rho_{for}^s}{\partial \gamma^s} = (1 - p)k_1^a \sqrt{\sum_{s'} g^{ss'} \rho_{tot}^{s'}} - k_2^a (\dot{\varepsilon}, T) \rho_{for}^s, \tag{11b}$$

$$\frac{\partial \rho_{rev}^{s^+}}{\partial \gamma^s} = -k_1^a \sqrt{\sum_{s'} g^{ss'} \rho_{tot}^{s'}} \left(\frac{\rho_{rev}^{s^+}}{\rho_0^s}\right)^m, \tag{12b}$$

$$\frac{\partial \rho_{rev}^{s^{-}}}{\partial \gamma^{s}} = p k_{1}^{\alpha} \sqrt{\sum_{s'} g^{ss'} \rho_{tot}^{s'}} - k_{2}^{\alpha}(\dot{\varepsilon}, T) \rho_{rev}^{s^{-}}, \tag{13b}$$

Along with these initial conditions

$$\rho_{fgr}^{s}(\gamma^{s}=0) = 4.1 \times 10^{12} \, m^{-2}, \rho_{rev}^{s^{+}}(\gamma^{s}=0) = 0 \text{ and } \rho_{rev}^{s^{-}}(\gamma^{s}=0) = 0.$$
 (14)

In the above equations, k_1^a is a fitting parameter controlling the rate of generation of dislocations, k_2^a is a temperature (T) and strain rate ($\dot{\varepsilon}$) sensitive parameter for dynamic recovery, p is a reversibility parameter in the range 0-1 but taken as 0.2, g^{ss} is another interaction matrix taken as $g^{ss}=1$ and $g^{ss}=1$ (Khadyko et al., 2016; Kocks et al., 1991; Teodosiu and Raphanel, 1991), m is a parameter governing the rate of dislocation recombination set to 0.5 (Wen et al., 2015), and ρ_0^s is the total dislocation density at the reversal (Kitayama et al., 2013).

The coefficient k_2^{α} is (Knezevic et al., 2013d; Knezevic et al., 2015)

$$\frac{k_2^{\alpha}}{k_1^{\alpha}} = \frac{\chi b^{\alpha}}{g^{\alpha}} \left(1 - \frac{k_B T}{D^{\alpha} (b^{\alpha})^3} ln \left(\frac{\dot{\varepsilon}}{\dot{\varepsilon}_0} \right) \right) \frac{k_2^{\alpha}}{k_1^{\alpha}} = \frac{\chi b^{\alpha}}{g^{\alpha}} \left(1 - \frac{kT}{D^{\alpha} b^3} ln \left(\frac{\dot{\varepsilon}}{\dot{\varepsilon}_0} \right) \right). \tag{15}$$

where, k_B is the Boltzmann constant, $\dot{\epsilon}_0 = 10^7$ is a reference strain-rate, g^{α} is a fitting parameter representing effective activation enthalpy, and D^{α} is a fitting parameter representing drag stress. The debris dislocation density evolves using (Knezevic et al., 2013e; Knezevic and Savage, 2014)

$$\frac{\partial \rho_{deb}}{\partial y^s} = q^a b^a \sqrt{\rho_{deb}} k_2^a(\dot{\epsilon}, T) \rho_{tot}^s, \tag{16}$$

where q^{α} is a fitting parameter determining the amount of dislocations that become debris. The debris dislocation density evolves from a small value of 0.1 m^{-2} .

References

- Abdullah, A., Samad, Z., 2013. An experimental investigation of springback of AA6061 aluminum alloy strip via V-bending process. In: IOP Conference Series: Materials Science and Engineering. IOP Publishing, p. 012069.
- Abdullah, A.B., Sapuan, S.M., Samad, Z., Aziz, N.A., 2012. A comprehensive review of experimental approaches used in the measurement of springback. Advances in Natural and Applied Sciences 6, 195+.
- Adnan, A.F., Abdullah, A.B., Samad, Z., 2017. Study of springback pattern of non-uniform thickness section based on V-bending experiment. Journal of Mechanical Engineering and Sciences 11, 2845–2855.
- Al-Harbi, H.F., Knezevic, M., Kalidindi, S.R., 2010. Spectral approaches for the fast computation of yield surfaces and first-order plastic property closures for polycrystalline materials with cubic-triclinic textures. CMC: Computers. Materials, & Continua 15. 153–172.
- Ardeljan, M., Savage, D.J., Kumar, A., Beyerlein, I.J., Knezevic, M., 2016. The plasticity of highly oriented nano-layered Zr/Nb composites. Acta Mater. 115, 189–203.
- Ashby, M.F., 1970. The deformation of plastically non-homogeneous materials. Phil. Mag. 21, 399–424.
- Bakhshivash, S., Sadeghi, B.M., Rahimi, F., Haghshenas, M., 2016. Effect of Bending Angle and Punch Tip Radius on Spring-Forward in an Al-Mg-Si Alloy.
- Barrett, T.J., Eghtesad, A., McCabe, R.J., Clausen, B., Brown, D.W., Vogel, S.C., Knezevic, M., 2019. A generalized spherical harmonics-based procedure for the interpolation of partial datasets of orientation distributions to enable crystal mechanics-based simulations. Materialia 6, 100328.
- Barrett, T.J., Knezevic, M., 2019. Deep drawing simulations using the finite element method embedding a multi-level crystal plasticity constitutive law: Experimental verification and sensitivity analysis. Comput. Methods Appl. Mech. Eng. 354, 245–270.
- Beyerlein, I.J., Tomé, C.N., 2008. A dislocation-based constitutive law for pure Zr including temperature effects. Int. J. Plast 24, 867–895.
- Boers, S.H.A., Schreurs, P.J.G., Geers, M.G.D., Levkovitch, V., Wang, J., Svendsen, B., 2010. Experimental characterization and model identification of directional hardening effects in metals for complex strain path changes. Int. J. Solids Struct. 47, 1361–1374.
- Chen, S., Liao, J., Xiang, H., Xue, X., Pereira, A.B., 2021. Pre-strain effect on twist springback of a 3D P-channel in deep drawing. J. Mater. Process. Technol. 287, 116224.
- Cheng, J., Green, D.E., Golovashchenko, S.F., 2017. Formability enhancement of DP600 steel sheets in electro-hydraulic die forming. J. Mater. Process. Technol. 244, 178, 180
- Chongthairungruang, B., Uthaisangsuk, V., Suranuntchai, S., Jirathearanat, S., 2012. Experimental and numerical investigation of springback effect for advanced high strength dual phase steel. Mater. Des. 39, 318–328.
- Cinar, Z., Asmael, M., Zeeshan, Q., Safaei, B., 2021. Effect of springback on A6061 sheet metal bending: a review. Jurnal Kejuruteraan 33, 13–26.
- Daroju, S., Kuwabara, T., Sharma, R., Fullwood, D.T., Miles, M.P., Knezevic, M., 2022. Experimental characterization and crystal plasticity modeling for predicting load reversals in AA6016-T4 and AA7021-T79. Int. J. Plast 153, 103292.
- Devincre, B., Kubin, L., Hoc, T., 2006. Physical analyses of crystal plasticity by DD simulations. Scr. Mater. 54, 741–746.
- Eghtesad, A., Barrett, T.J., Knezevic, M., 2018. Compact reconstruction of orientation distributions using generalized spherical harmonics to advance large-scale crystal plasticity modeling: Verification using cubic, hexagonal, and orthorhombic polycrystals. Acta Mater. 155, 418–432.
- El-Madhoun, Y., Mohamed, A., Bassim, M., 2003. Cyclic stress-strain response and dislocation structures in polycrystalline aluminum. Mater. Sci. Eng. A 359, 220–227.

- Eshelby, J.D., 1957. The determination of the elastic field of an ellipsoidal inclusion, and related problems. Proc. R. Soc. Lond. A 241, 376–396.
- Feng, Z., Yoon, S.-Y., Choi, J.-H., Barrett, T.J., Zecevic, M., Barlat, F., Knezevic, M., 2020. A comparative study between elasto-plastic self-consistent crystal plasticity and anisotropic yield function with distortional hardening formulations for sheet metal forming. Mech. Mater. 148, 103422.
- Feng, Z., Mamros, E.M., Ha, J., Kinsey, B.L., Knezevic, M., 2021a. Modeling of plasticity-induced martensitic transformation to achieve hierarchical, heterogeneous, and tailored microstructures in stainless steels. CIRP J. Manuf. Sci. Technol. 33, 389–397
- Feng, Z., Zecevic, M., Knezevic, M., 2021b. Stress-assisted $(\gamma \rightarrow \alpha')$ and strain-induced $(\gamma \rightarrow \epsilon \alpha')$ phase transformation kinetics laws implemented in a crystal plasticity model for predicting strain path sensitive deformation of austenitic steels. Int. J. Plast 136, 102807.
- Feng, Z., Pokharel, R., Vogel, S.C., Lebensohn, R.A., Pagan, D., Zepeda-Alarcon, E., Clausen, B., Martinez, R., Gray, G.T., Knezevic, M., 2022. Crystal plasticity modeling of strain-induced martensitic transformations to predict strain rate and temperature sensitive behavior of 304 L steels: Applications to tension, compression, torsion, and impact. Int. J. Plast 156, 103367.
- Ferreri, N.C., Feng, Z., Savage, D.J., Brown, D.W., Clausen, B., Sisneros, T.A., Knezevic, M., 2022. In-situ high-energy X-ray diffraction and crystal plasticity modeling to predict the evolution of texture, twinning, lattice strains and strength during loading and reloading of beryllium. Int. J. Plast 150, 103217.
- Field, D.P., Trivedi, P.B., Wright, S.I., Kumar, M., 2005. Analysis of local orientation gradients in deformed single crystals. Ultramicroscopy 103, 33–39.
- Franciosi, P., Zaoui, A., 1982. Multislip in f.c.c. crystals a theoretical approach compared with experimental data. Acta Metall. 30, 1627–1637.
- Grizelj, B., Cumin, J., Grizelj, D., 2010. Effect of spring-back and spring-forward in V-die bending of St1403 sheet metal plates. Strojarstvo: časopis za teoriju i praksu u strojarstvu 52, 181–186.
- Hoc, T., Devincre, B., Kubin, L., 2004. Deformation stage I of FCC crystals: Constitutive modelling. In: 25th Riso International Symposium on Materials Science 2004, pp. 43–59.
- Hu, Y., Curtin, W.A., 2021. Modeling peak-aged precipitate strengthening in Al-Mg-Si alloys. J. Mech. Phys. Solids 151, 104378.
- Joo, M., Wi, M.-S., Yoon, S.-Y., Lee, S.-Y., Barlat, F., Tome, C., Jeon, B., Jeong, Y., 2023. A crystal plasticity finite element analysis of the effect of pre-strain on springback. Int. J. Mech. Sci. 237, 107796.
- Khadyko, M., Dumoulin, S., Cailletaud, G., Hopperstad, O.S., 2016. Latent hardening and plastic anisotropy evolution in AA6060 aluminium alloy. Int. J. Plast 76, 51–74.
- Kitayama, K., Tomé, C.N., Rauch, E.F., Gracio, J.J., Barlat, F., 2013. A crystallographic dislocation model for describing hardening of polycrystals during strain path changes. Application to low carbon steels. Int. J. Plast 46, 54–69.
- Knezevic, M., Beyerlein, I.J., 2018. Multiscale Modeling of Microstructure-Property Relationships of Polycrystalline Metals during Thermo-Mechanical Deformation. Adv. Eng. Mater. 20, 1700956.
- Knezevic, M., Landry, N.W., 2015. Procedures for reducing large datasets of crystal orientations using generalized spherical harmonics. Mech. Mater. 88, 73–86.
- Knezevic, M., Capolungo, L., Tomé, C.N., Lebensohn, R.A., Alexander, D.J., Mihaila, B., McCabe, R.J., 2012. Anisotropic stress-strain response and microstructure evolution of textured α-uranium. Acta Mater. 60, 702–715.
- Knezevic, M., Beyerlein, I.J., Brown, D.W., Sisneros, T.A., Tomé, C.N., 2013a.
 A polycrystal plasticity model for predicting mechanical response and texture evolution during strain-path changes: Application to beryllium. Int. J. Plast 49, 125.
- Knezevic, M., Beyerlein, I.J., Nizolek, T., Mara, N.A., Pollock, T.M., 2013b. Anomalous basal slip activity in zirconium under high-strain deformation. Mater. Res. Lett. 1, 133–140.

- Knezevic, M., Lebensohn, R.A., Cazacu, O., Revil-Baudard, B., Proust, G., Vogel, S.C., Nixon, M.E., 2013c. Modeling bending of α-titanium with embedded polycrystal plasticity in implicit finite elements. Mater. Sci. Eng. A 564, 116–126.
- Knezevic, M., Savage, D.J., 2014. A high-performance computational framework for fast crystal plasticity simulations. Comput. Mater. Sci. 83, 101–106.
- Knezevic, M., McCabe, R.J., Lebensohn, R.A., Tomé, C.N., Liu, C., Lovato, M.L., Mihaila, B., 2013d. Integration of self-consistent polycrystal plasticity with dislocation density based hardening laws within an implicit finite element framework: Application to low-symmetry metals. J. Mech. Phys. Solids 61, 2034–2046.
- Knezevic, M., McCabe, R.J., Tomé, C.N., Lebensohn, R.A., Chen, S.R., Cady, C.M., Gray Iii, G.T., Mihaila, B., 2013e. Modeling mechanical response and texture evolution of curanium as a function of strain rate and temperature using polycrystal plasticity. Int. J. Plast 43, 70–84.
- Knezevic, M., Beyerlein, I.J., Lovato, M.L., Tomé, C.N., Richards, A.W., McCabe, R.J., 2014. A strain-rate and temperature dependent constitutive model for BCC metals incorporating non-Schmid effects: Application to tantalum–tungsten alloys. Int. J. Plast 62, 93–104.
- Knezevic, M., Zecevic, M., Beyerlein, I.J., Bingert, J.F., McCabe, R.J., 2015. Strain rate and temperature effects on the selection of primary and secondary slip and twinning systems in HCP Zr. Acta Mater. 88, 55–73.
- Knezevic, M., Crapps, J., Beyerlein, I.J., Coughlin, D.R., Clarke, K.D., McCabe, R.J., 2016.
 Anisotropic modeling of structural components using embedded crystal plasticity
 constructive laws within finite elements. Int. J. Mech. Sci. 105, 227–238.
- constructive laws within finite elements. Int. J. Mech. Sci. 105, 227–238.

 Knockaert, R., Chastel, Y., Massoni, E., 2000. Rate-independent crystalline and
- polycrystalline plasticity, application to FCC materials. Int. J. Plast 16, 179–198. Kocks, U.F., Mecking, H., 1981. Kinetics of Flow and Strain-Hardening. Acta Metall. 29, 1865–1875.
- Kocks, U.F., Franciosi, P., Kawai, M., 1991. A Forest Model of Latent Hardening and its Application to Polycrystal Deformations. Textures Microstructures 14, 1103–1114.
- Kuwabara, T., Mori, T., Asano, M., Hakoyama, T., Barlat, F., 2017. Material modeling of 6016-O and 6016-T4 aluminum alloy sheets and application to hole expansion forming simulation. Int. J. Plast 93, 164-186.
- Li, K.P., Carden, W.P., Wagoner, R.H., 2002. Simulation of springback. Int. J. Mech. Sci. 44, 103–122.
- Liao, J., Chen, S., Xue, X., Xiang, H., 2020. On twist springback of a curved channel with pre-strain effect. Int. J. Lightweight Mater. Manuf. 3, 108–112.
- Lipinski, P., Berveiller, M., 1989. Elastoplasticity of micro-inhomogeneous metals at large strains. Int. J. Plast 5, 149–172.
- Madec, R., Devincre, B., Kubin, L., Hoc, T., Rodney, D., 2003. The role of collinear interaction in dislocation-induced hardening. Science 301, 1879–1882.
- Moan, G., Embury, J., 1979. A study of the bauschinger effect in Al Cu alloys. Acta Metall. 27, 903–914.
- Muhammad, W., Brahme, A.P., Kang, J.D., Mishra, R.K., Inal, K., 2017. Experimental and numerical investigation of texture evolution and the effects of intragranular backstresses in aluminum alloys subjected to large strain cyclic deformation. Int. J. Plast 93, 137–163.
- Nagtegaal, J.C., Veldpaus, F.E., 1984. On the implementation of finite strain plasticity equations in a numerical model. Numer. Methods Ind. Forming Processes 351–371.
- Neil, C.J., Wollmershauser, J.A., Clausen, B., Tomé, C.N., Agnew, S.R., 2010. Modeling lattice strain evolution at finite strains and experimental verification for copper and stainless steel using in situ neutron diffraction. Int. J. Plast 26, 1772–1791.
- Rakshit, R., Sarkar, A., Panda, S.K., Mandal, S., 2022. Influence of out-of-plane stretch forming induced different strain paths on micro-texture evolution, slip system activity and Taylor factor distribution in Al-Li alloy. Mat Sci Eng a-Struct 830.
- Ruggles, Fullwood, 2015. OpenXY (Version1.0): https://github.com/BYU-MicrostructureOfMaterials/OpenXY, Brigham Young University.

- Sato, Y.S., Urata, M., Kokawa, H., 2002. Parameters controlling microstructure and hardness during friction-stir welding of precipitation-hardenable aluminum alloy 6063. Metall. Mater. Trans. A 33, 625–635.
- Sharma, R., Sargeant, D., Daroju, S., Kenezevic, M., Miles, M.P., Fullwood, D.T., 2022. Multi-strain path deformation behavior of AA6016-T4: Experiments and crystal plasticity modeling. Int. J. Solids Struct. 111536.
- Shen, Z., Wagoner, R.H., Clark, W.A.T., 1988. Dislocation and grain boundary interactions in metals. Acta Metall. 36, 3231–3242.
- Stoltz, R., Pelloux, R., 1974. Cyclic deformation and bauschinger effect in Al Cu Mg alloys. Scr. Metall. 8, 269–275.
- Stoltz, R.E., Pelloux, R.M., 1976. The Bauschinger effect in precipitation strengthened aluminum alloys. Metall. Trans. A 7, 1295–1306.
- Teodosiu, C., Raphanel, J.L., 1991. Finite element simulations of large elastoplastic deformations of multicrystals. In: Proceedings of the International Seminar MECAMAT91, pp. 153–168.
- Thipprakmas, S., Rojananan, S., 2008. Investigation of spring-go phenomenon using finite element method. Mater. Des. 29, 1526–1532.
- Turner, P.A., Tomé, C.N., 1994. A study of residual stresses in Zircaloy-2 with rod texture. Acta Metall. Mater. 42, 4143–4153.
- Wagoner, R.H., Lim, H., Lee, M.-G., 2013. Advanced Issues in springback. Int. J. Plast 45, 3–20.
- Wen, W., Borodachenkova, M., Tomé, C.N., Vincze, G., Rauch, E.F., Barlat, F., Grácio, J. J., 2015. Mechanical behavior of Mg subjected to strain path changes: Experiments and modeling. Int. J. Plast 73, 171–183.
- Wollmershauser, J.A., Clausen, B., Agnew, S.R., 2012. A slip system-based kinematic hardening model application to in situ neutron diffraction of cyclic deformation of austenitic stainless steel. Int. J. Fatigue 36, 181–193.
- Yoshida, F., Uemori, T., Fujiwara, K., 2002. Elastic-plastic behavior of steel sheets under in-plane cyclic tension-compression at large strain. Int. J. Plast 18, 633-659.
- Yue, Z., Qi, J., Zhao, X., Badreddine, H., Gao, J., Chu, X., 2018. Springback Prediction of Aluminum Alloy Sheet under Changing Loading Paths with Consideration of the Influence of Kinematic Hardening and Ductile Damage. Metals 2018, Vol. 8, Page 950 8, 950-950.
- Zecevic, M., Knezevic, M., 2015. A dislocation density based elasto-plastic self-consistent model for the prediction of cyclic deformation: Application to Al6022-T4. Int. J. Plast 72, 200-217.
- Zecevic, M., Knezevic, M., 2018. Latent hardening within the elasto-plastic selfconsistent polycrystal homogenization to enable the prediction of anisotropy of AA6022-T4 sheets. Int. J. Plast 105, 141–163.
- Zecevic, M., Knezevic, M., 2019. An implicit formulation of the elasto-plastic selfconsistent polycrystal plasticity model and its implementation in implicit finite elements. Mech. Mater. 136, 103065.
- Zecevic, M., Knezevic, M., Beyerlein, I.J., Tomé, C.N., 2015. An elasto-plastic self-consistent model with hardening based on dislocation density, twinning and detwinning: Application to strain path changes in HCP metals. Mater. Sci. Eng. A 638, 262-274
- Zecevic, M., Korkolis, Y.P., Kuwabara, T., Knezevic, M., 2016. Dual-phase steel sheets under cyclic tension–compression to large strains: experiments and crystal plasticity modeling. J. Mech. Phys. Solids 96, 65–87.
- Zecevic, M., Upadhyay, M.V., Polatidis, E., Panzner, T., Van Swygenhoven, H., Knezevic, M., 2019. A crystallographic extension to the Olson-Cohen model for predicting strain path dependence of martensitic transformation. Acta Mater. 166, 386-401
- Zhang, Z., Hu, S., 1998. Stress and residual stress distributions in plane strain bending. Int. J. Mech. Sci. 40, 533–543.